Joint Estimation and Correction of Geometric Distortions for EPI functional MRI using Harmonic Retrieval

Hien M. Nguyen, Bradley P. Sutton, *Member, IEEE,* Robert L. Morrison, Jr., *Member, IEEE,* Minh N. Do, *Senior Member, IEEE*

***Abstract*—Magnetic Resonance Imaging (MRI) uses applied spatial variations in the magnetic field to encode spatial position. Therefore, non-uniformities in the main magnetic field can cause image distortions. In order to correct the image distortions, it is desirable to simultaneously acquire data with a field map in registration. We propose a joint estimation (JE) framework with a fast, non-iterative approach using harmonic retrieval (HR) methods, combined with a multi-echo EPI acquisition. The connection with HR establishes an elegant framework to solve the JE problem through a sequence of one dimensional HR problems in which efficient solutions are available. We also derive the condition on the smoothness of the field map in order for HR techniques to recover the image with high signal-to-noise ratio. Compared to other dynamic field mapping methods, this method is not constrained by the absolute level of the field inhomogeneity over the slice, but relies on a generous pixel-to-pixel smoothness. Moreover, this method can recover image, field map, and T2* map simultaneously.**

***Index Terms*—Image reconstruction, field inhomogeneity, functional MRI, EPI, harmonic retrieval, geometric distortions.**

I. INTRODUCTION

A. Motivation

CONVENTIONAL image reconstruction in MRI relies on a Fourier transform relationship between the acquired data and the image of the object. Given a continuous object with contrast-weighted spin density represented by $f(\boldsymbol{r})$ and a specific *k*-space trajectory $\boldsymbol{k}$, which is a function of time t (however for our convenience we will write t as a function of $\boldsymbol{k}$) and neglecting field inhomogeneity the signal $s(\boldsymbol{k})$ during the readout can be written as [1]

$$s(\boldsymbol{k}) = \int f(\boldsymbol{r}) e^{-i2\pi(\boldsymbol{k}\cdot\boldsymbol{r})} d\boldsymbol{r}, \tag{1}$$

However, in practice the magnetic field across the object being imaged is not homogeneous, which leads to distortions in the resulting image. Due to magnetic susceptibility differences near air/tissue interfaces, an inhomogeneous magnetic field exists in many regions of the body and brain [2], [3]. This in turn leads to an off-resonance in the frequency and the relation (1) between MRI data and object is no longer a Fourier transform [4]–[7]:

$$s(\boldsymbol{k}) = \int f(\boldsymbol{r}) e^{-i\omega(\boldsymbol{r})t(\boldsymbol{k})} e^{-t(\boldsymbol{k})/T_2^*(\boldsymbol{r})} e^{-i2\pi(\boldsymbol{k}\cdot\boldsymbol{r})} d\boldsymbol{r}, \tag{2}$$

where $\omega(\boldsymbol{r})$ is a map of the inhomogeneity of the magnetic field, i.e., a *field map*,[1] and $T_2^*(\boldsymbol{r})$ term models the destruction of transverse magnetization in the spatial domain. Based on (2) we notice that the long readout time of single-shot acquisitions such as echo-planar imaging (EPI) or spiral imaging leads to a significant diversion from the standard model (1) and causes image distortion [4], [8]. As field inhomogeneity scales with magnetic field, the current trend towards higher field systems makes potential image distortions and correction methods vital to continued accurate imaging. In addition, fast, single-shot acquisitions make scans very sensitive to magnetic susceptibility differences at air/tissue interfaces in the brain [3]. This can cause severe distortions in functional imaging of the brain.

As an example of the impact of magnetic field inhomogeneity, consider functional magnetic resonance imaging (fMRI), which plays an important role in studying localized brain function, both in examining healthy cognitive function and in clinical patient groups. Geometric distortions in EPI and blurring effects in spiral imaging caused by field inhomogeneity severely affect predictions about the subject's brain [see Fig. 5(c) and Fig. 6(c)]. Many different methods to correct the distortions have been proposed [9]–[15]. Most of these methods involve two steps: estimating magnetic field variation and then compensating for this variation during image reconstruction. The methods differ both in how they estimate the field map and how they use that information to correct the images. A common method measures the field map by acquiring two images (which are called the *reference*

H. M. Nguyen is with the Department of Electrical and Computer Engineering, University of Illinois at Urbana-Champaign, Urbana IL 61801 (email: hnguyen6@illinois.edu).

B. P. Sutton is with the Bioengineering Department and the Beckman Institute, University of Illinois at Urbana-Champaign, Urbana IL 61801 (email: bsutton@illinois.edu).

R. L. Morrison was with the Department of Electrical and Computer Engineering, University of Illinois at Urbana-Champaign, Urbana IL 61801, he is now with the MIT Lincoln Laboratory, Lexington MA 02420 (email: rlmorris@illinois.edu).

M. N. Do is with the Department of Electrical and Computer Engineering, the Coordinated Science Laboratory, and the Beckman Institute, University of Illinois at Urbana-Champaign, Urbana IL 61801 (email: minhdo@illinois.edu).

This work was supported in part by the US National Science Foundation under Grant CCF-0430877 and a Vietnam Education Foundation fellowship.

[1] In our notations, we assume that the field map is measured in rad/s.

images) with slightly different echo times (TEs), which are times at which the echoes appear, and computing the field map based on their phase difference divided by difference in TEs [7]. In the case of a rectilinear trajectory, such as echo planar imaging (EPI), once the field map is found, correction of the images can be accomplished by shifting image pixels and correcting their intensities based on the estimated field map [9]. This conventional method for finding the field map from reference images implicitly assumes that magnetic field inhomogeneity is static, an assumption that is violated due to subject motion or physiological changes [4]. To overcome this problem Nayak and Nishimura [6] used multi-shot acquisition to generate multiple reference images, each subsequent shot having a delayed TE. Yet, this approach is limited by its temporal resolution (multi-shot) and by the global range of the field map that can be recovered. In addition, the approach estimates distorted field maps that are used to correct the images. Some other methods try to bypass estimation of the field map. For example, in [2] and [16] two images of the same object are acquired with preparation and readout gradients altered by some ratio α. The corrected image is produced by combining and rectifying these two acquired images pixel by pixel. However, such rectification method requires identification of an initial pair of corresponding points. Another recent approach suggested by [4], [17] is to combine the two steps together: reconstruct the undistorted image and field map *simultaneously* from the acquired data. This problem is called the *joint estimation* (JE) problem. The advantages of the JE approach is that it needs only single shot excitation to estimate the field map dynamically and does not require acquiring reference images, thus bypassing the problem of the displacement error between these images. Moreover, the field map is estimated dynamically, allowing to account for motion or physiological changes; it is also in registration with the data and undistorted by field inhomogeneity effects, so there is no need to realign the field map with the data prior to being able to apply a correction scheme.

B. Goal of This Work

In [4] the JE problem was solved as a nonlinear least-squares optimization problem with regularization using iterative conjugate gradients (CG) method. This method requires an initial guess of the field map for the first iteration and it is computationally expensive. In this work, we propose a non-iterative approach to the JE problem using *harmonic retrieval* (HR) techniques. We show that under certain approximation the JE problem can be treated as a sequence of 1D HR problems in which efficient solutions are available [18]. Thus, we present a method that can dynamically estimate the field map non-iteratively. Advantages of this approach include low complexity and robustness to incorrect local minima solutions of the CG method. In addition, no prior information for field map is needed. We concentrate on the case when k-space trajectory is EPI, which is commonly used for functional imaging, and we modify the EPI trajectory to be a multi-echo acquisition. We also point out a condition on the smoothness of the original field map and characterize the restoration quality as a function of field map. This condition shows that our approach is not limited by the absolute field map range that we can afford. In addition, experimental results show that the restored image does not suffer from geometric distortions and has much reduced signal loss artifact compared to the methods that do not account for the field map.

The outline of the rest of the paper is as follows. Section II recalls the mathematical formulation of the JE problem and describes continuous and discrete equations of the problem [4]. Section III shows the key contribution of our work: how to solve the JE problem using HR techniques, which gives the advantages that we discussed above, and a generous criteria for this approach to work. Section IV considers practical issues including choosing an appropriate HR technique for the JE problem and designing a suitable data acquisition scheme. Section V presents experimental results with simulated and real data. Section VI presents our conclusions.

II. PROBLEM SETUP

Given the signal during the readout $s(t)$ with specific k-space trajectory $\boldsymbol{k}(t)$, the JE problem recovers the image $f(\boldsymbol{r})$ and the field map $w(\boldsymbol{r})$, both satisfying (2) in the presence of the T_2^* decay.

We use $\boldsymbol{r} = (x, y)$ to denote a location in the image space; $\boldsymbol{k} = (k_x, k_y)$ to denote a location in the k-space; while $\boldsymbol{n} = [n_1, n_2]$ and $\boldsymbol{m} = [m_1, m_2]$ are indexes for the discrete locations of $\boldsymbol{r}$ and $\boldsymbol{k}$, respectively.

Assume the object has size $N_1 \times N_2$. We expand continuous image $f(\boldsymbol{r})$ by linear expansion using the box function

$$\varphi_{\mathbf{T}}(\boldsymbol{r}) = \begin{cases} 1, & 0 \le x < T_1,\ 0 \le y < T_2 \\ 0, & \text{else} \end{cases} \tag{3}$$

and its translated versions $\{\varphi_{\mathbf{T}}(\boldsymbol{r} - \boldsymbol{n} \odot \boldsymbol{T}) = \varphi_{\mathbf{T}}(x - n_1 T_1, y - n_2 T_2)\}_{\boldsymbol{n} \in \boldsymbol{Z}^2}$, where operator $\odot$ denotes Schur-Hadamard (element by element) matrix product. That is

$$f(\boldsymbol{r}) = \sum_{\boldsymbol{n}} f[\boldsymbol{n}] \varphi_{\mathbf{T}}(\boldsymbol{r} - \boldsymbol{n} \odot \boldsymbol{T}) \tag{4}$$

or we have $f(\boldsymbol{r}) = f[\boldsymbol{n}]$ for $\boldsymbol{r} \in V_{\boldsymbol{n}}$, where $V_{\boldsymbol{n}}$ denotes the voxel region $[n_1 T_1, (n_1 + 1)T_1] \times [n_2 T_2, (n_2 + 1)T_2]$ of size $T_1 \times T_2$ indexed by $\boldsymbol{n} = (n_1, n_2)$. And similarly, we can approximate the continuous field map $\omega(\boldsymbol{r})$ and T_2^* decay map $T_2^*(\boldsymbol{r})$ with discrete signals $\omega[\boldsymbol{n}]$ and $T_2^*[\boldsymbol{n}]$, respectively, using the same box function. Notice that here we assume constant intensity within a voxel for both the image and field map, which ignores the possibility of intra-voxel gradients in the field inhomogeneity.

Substituting (4) into (2) yields

$$\begin{aligned} s(\boldsymbol{k}) \quad = \quad & \sum_{\boldsymbol{n}} f[\boldsymbol{n}] \int \varphi_{\mathbf{T}}(\boldsymbol{r} - \boldsymbol{T} \odot \boldsymbol{n}) e^{-i\omega(\boldsymbol{r}) t(\boldsymbol{k})} \\ & \times e^{-t(\boldsymbol{k})/T_2^*(\boldsymbol{r})} e^{-i2\pi \boldsymbol{k} \cdot \boldsymbol{r}} d\boldsymbol{r}. \end{aligned} \tag{5}$$

Since $\varphi_{\mathbf{T}}(\boldsymbol{r} - \boldsymbol{n} \odot \boldsymbol{T}) = 1$ when $\boldsymbol{r} \in V_{\boldsymbol{n}}$ and 0 else, we only need to consider $\boldsymbol{r} \in V_{\boldsymbol{n}}$ in the integral in (5). In that region

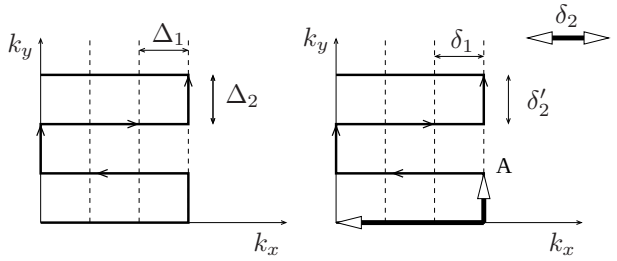

Fig. 1. Left: EPI sampling trajectory in k-space: Δ_1, Δ_2 are sampling intervals in k-space. Right: EPI sampling trajectory in time domain: δ_1, δ_2' are time delays between samples along the k_x and k_y dimensions, respectively; δ_2 is a time delay from the origin until point A.

we have $\omega(\boldsymbol{r}) = \omega[\boldsymbol{n}]$ and $T_2^*(\boldsymbol{r}) = T_2^*[\boldsymbol{n}]$, which yields

$$\begin{aligned} s(\boldsymbol{k}) &= \sum_{\boldsymbol{n}} f[\boldsymbol{n}] e^{-i\omega[\boldsymbol{n}]t(\boldsymbol{k})} e^{-t(\boldsymbol{k})/T_2^*[\boldsymbol{n}]} \\ &\quad \times \int \varphi_{\mathbf{T}}(\boldsymbol{r} - \boldsymbol{T} \odot \boldsymbol{n}) e^{-i2\pi \boldsymbol{k}\cdot\boldsymbol{r}} d\boldsymbol{r} \\ &= \sum_{\boldsymbol{n}} f[\boldsymbol{n}] e^{-i\omega[\boldsymbol{n}]t(\boldsymbol{k})} e^{-t(\boldsymbol{k})/T_2^*[\boldsymbol{n}]} \Phi_{\mathbf{T}}(\boldsymbol{k}) \\ &\quad \times e^{-i2\pi \boldsymbol{k}\cdot(\boldsymbol{T}\odot\boldsymbol{n})}, \end{aligned}$$

where $\Phi_{\mathbf{T}}(\boldsymbol{k}) \stackrel{\text{def}}{=} \int \varphi_{\mathbf{T}}(\boldsymbol{r}) e^{-i2\pi\boldsymbol{k}\cdot\boldsymbol{r}} d\boldsymbol{r}$ is the Fourier transform of $\varphi_{\mathbf{T}}(\boldsymbol{r})$. Thus, the discretized form of the JE problem is given by the following equation

$$\begin{aligned} \overline{s}(\boldsymbol{k}) \stackrel{\text{def}}{=} \frac{s(\boldsymbol{k})}{\Phi_{\mathbf{T}}(\boldsymbol{k})} &= \sum_{\boldsymbol{n}} f[\boldsymbol{n}] e^{-i\omega[\boldsymbol{n}]t(\boldsymbol{k})} e^{-t(\boldsymbol{k})/T_2^*[\boldsymbol{n}]} \\ &\quad \times e^{-i2\pi \boldsymbol{k}\cdot(\boldsymbol{T}\odot\boldsymbol{n})}. \end{aligned} \tag{6}$$

III. PROPOSED APPROACH

In this section we show the main contribution of this work: realizing and building a bridge between JE problem and another problem, called *Harmonic Retrieval* (HR), which can be solved using existing signal processing techniques.

A. Connecting JE to HR Problem

We assume the particular case of an EPI trajectory $\boldsymbol{k}$ as described in Fig. 1. Denote those k-space lines along which the data is acquired from left to the right as *forward* lines and lines along which the data is acquired from right to the left as *backward* lines.

Let δ_1, δ_2' be the time delays and Δ_1, Δ_2 be the distances in k-space between two consecutive samples of the EPI trajectory along frequency-encoding (k_x) and phase-encoding axes (k_y), respectively, as shown in Fig. 1. The total number of samples along the horizontal and vertical axes is M_1 and M_2, respectively. We also denote δ_2 to be a time delay between sampling the centers of adjacent horizontal lines, *i.e.*, echo spacing. Hence, the following relation holds

$$\delta_2 = \delta_1(M_1 - 1) + \delta_2'. \tag{7}$$

Next, we need to discretize continuous k-space trajectory $\boldsymbol{k}$ and the related timing function $t(\boldsymbol{k})$. The discrete function $\boldsymbol{k}[\boldsymbol{m}]$ has one single form for both forward and backward lines. For simplicity in derivation and without loss of generality through the Fourier shift theorem, we assume that k-space sampling starts from the origin as it is depicted in Fig. 1:

$$\boldsymbol{k}[\boldsymbol{m}] = \begin{bmatrix} m_1\Delta_1 \\ m_2\Delta_2 \end{bmatrix}. \tag{8}$$

The continuous function $t(\boldsymbol{k})$ takes different discrete forms $t[\boldsymbol{m}]$ depending on the kind of the k-space line that we are considering. From the figure we see that the timing delay for the samples lying on forward lines (m_2 is even) and backward lines (m_2 is odd) is expressed differently as the following:

$$t[\boldsymbol{m}] = \begin{cases} m_1\delta_1 + m_2\delta_2, & m_2 \text{ even}, \\ (M_1 - 1 - m_1)\delta_1 + m_2\delta_2, & m_2 \text{ odd}. \end{cases} \tag{9}$$

Forward lines: Substituting (8) and (9) into (6) while normalizing k-space locations by $\frac{1}{FOV}$ and spatial locations by FOV, which leads to $T_1 = 1/N_1$ and $T_2 = 1/N_2$, we obtain

$$\begin{aligned} \overline{s}[\boldsymbol{m}] &= \sum_{\boldsymbol{n}} f[\boldsymbol{n}] e^{-i\omega[\boldsymbol{n}](m_1\delta_1 + m_2\delta_2)} \\ &\quad \times e^{-(m_1\delta_1 + m_2\delta_2)/T_2^*[\boldsymbol{n}]} \\ &\quad \times e^{-i(\frac{2\pi}{N_1} m_1\Delta_1 n_1 + \frac{2\pi}{N_2} m_2\Delta_2 n_2)}. \end{aligned} \tag{10}$$

In practice, the time interval δ_1 between two samples along the horizontal k-space line is two orders of magnitude smaller than the time δ_2 needed for the gradient to change its direction and go to the next line, therefore $\delta_1 \ll \delta_2$. Hence, we can assume that $\omega[\boldsymbol{n}]\delta_1 \approx 0$ and $\delta_1/T_2^*[\boldsymbol{n}] \approx 0$. The first approximation is widely used for EPI [9] and the second approximation is easily satisfied noting that the typical sampling readout δ_1 is about 5 μs, whereas $T_2^*[\boldsymbol{n}]$ is usually in the range from 10 ms to 100 ms. Setting $\Delta_1 = 1$ and taking inverse DFT of both sides of the equation (10) along horizontal m_1 direction, we get

$$\begin{aligned} \hat{s}[n_1, m_2] &= \sum_{n_2=0}^{N_2-1} f[n_1, n_2] \\ &\quad \times \left(e^{-\delta_2/T_2^*[n_2]} e^{-i(\omega[\boldsymbol{n}]\delta_2 + \frac{2\pi}{N_2}\Delta_2 n_2)} \right)^{m_2}, \\ m_2 &= 0, ..., M_2 - 1, \end{aligned} \tag{11}$$

where $\hat{s}[n_1, m_2] \stackrel{\text{def}}{=} DFT_{N_1}^{-1}\{\overline{s}[m_1, m_2]\}$. For a fixed n_1 denote

$$\begin{aligned} a_n &= f[n_1, n], \\ z_n &= e^{-\delta_2/T_2^*[n_1,n]} e^{-i(\omega[n_1,n]\delta_2 + \frac{2\pi}{N}\Delta_2 n)} \\ \tau_m &= \hat{s}[n_1, m_2], \end{aligned} \tag{12}$$

where $n = n_2$, $N = N_2$, $m = m_2$, $M = M_2$. Then we can rewrite (11) as

$$\tau_m = \sum_{n=0}^{N-1} a_n z_n^m, \quad m = 0, ..., M - 1. \tag{13}$$

Backward lines: similarly, we get the following equation for

backward case:

$$\begin{aligned}\overline{s}[\boldsymbol{m}] &= \sum_{\boldsymbol{n}} f[\boldsymbol{n}] e^{-i(\omega[\boldsymbol{n}](M_1-1-m_1)\delta_1+m_2\delta_2)} \\ &\quad \times e^{-((M_1-1-m_1)\delta_1+m_2\delta_2)/T_2^*[\boldsymbol{n}]} \\ &\quad \times e^{-i(\frac{2\pi}{N_1}m_1\Delta_1 n_1+\frac{2\pi}{N_2}m_2\Delta_2 n_2)}. \end{aligned} \quad (14)$$

Assuming again that $w[\boldsymbol{n}]\delta_1 \approx 0$ and $\delta_1/T_2^*[\boldsymbol{n}] \approx 0$, we obtain the same problem formulation as equation (11) in forward case. As a result, with this assumption, the forward and backward lines can be treated in the same way.

In practice, since k-space coverage is symmetric, the acquired data is $s[\tilde{k_1}, \tilde{k_2}]$, where $-\frac{N_1}{2} \leq \tilde{k_1} < \frac{N_1}{2}$ and $-\frac{N_2}{2} \leq \tilde{k_2} < \frac{N_2}{2}$. In this case we get the same derivation except that the shift in k-space, $s[k_1 - \frac{N}{2}, k_2 - \frac{N}{2}]$ leads to a modulation term in the spatial domain: $\tilde{f}[\boldsymbol{n}] = f[\boldsymbol{n}]e^{-i\pi n_1}e^{-i\pi n_2}$.

B. Harmonic Retrieval Methods

In (13), $\{\tau_m\}$ are the given data samples $\{\hat{s}[n_1, m]\}$, whereas $\{a_n\}$ and $\{z_n\}$ are unknowns. Solving (13) is precisely the 1D harmonic retrieval (HR), which can be solved when $M \geq 2N$ (M complex data samples τ_m, $2N$ complex unknowns a_n and z_n). Given the complex values z_n, we can recover the field map and T_2^* map by noting that

$$\begin{aligned} |z_n| &= e^{-\delta_2/T_2^*[n_1,n]}, \\ \angle z_n &= -\omega[n_1, n]\delta_2 - \frac{2\pi}{N}\Delta_2 n. \end{aligned} \quad (15)$$

The HR problem (11) can be solved by noting that $\{z_n\}$ are roots of the characteristic polynomial [19], [20]

$$z^N + p_{N-1}z^{N-1} + ... + p_1 z^1 + p_0 z^0 = 0, \quad (16)$$

where the polynomial coefficients p_n, $n = 0, ..., N-1$ are solutions of the following matrix equation:

$$\underbrace{\begin{bmatrix} \tau_0 & \tau_1 & \cdots & \tau_{N-1} \\ \tau_1 & \tau_2 & \cdots & \tau_N \\ & \cdots & & \\ \tau_{M-N-1} & \tau_{M-N} & \cdots & \tau_{M-2} \end{bmatrix}}_{\boldsymbol{A}} \underbrace{\begin{bmatrix} p_0 \\ p_1 \\ \cdots \\ p_{N-1} \end{bmatrix}}_{\boldsymbol{p}} = -\underbrace{\begin{bmatrix} \tau_N \\ \tau_{N+1} \\ \cdots \\ \tau_{M-1} \end{bmatrix}}_{\boldsymbol{b}}. \quad (17)$$

Solving this equation gives coefficients $\{p_n\}$, from which we can find $\{z_n\}$ as roots of the polynomial in (16). Once $\{z_n\}$ are found, the corresponding unknowns $\{a_n\}$ can be easily computed by solving the following linear equation with a Vandermonde matrix $\boldsymbol{Z}$:

$$\begin{bmatrix} \tau_0 \\ \tau_1 \\ \cdots \\ \tau_{M-1} \end{bmatrix} = \underbrace{\begin{bmatrix} z_0^0 & \cdots & z_{N-1}^0 \\ z_0^1 & \cdots & z_{N-1}^1 \\ & \cdots & \\ z_0^{M-1} & \cdots & z_{N-1}^{M-1} \end{bmatrix}}_{\boldsymbol{Z}} \begin{bmatrix} a_0 \\ a_1 \\ \cdots \\ a_{N-1} \end{bmatrix}. \quad (18)$$

The total complexity of the proposed approach using HR technique for a fixed n_1 is $O(N_2^2)$ by exploiting the Toeplitz and Vandermonde structures of the matrices $\boldsymbol{A}$ and $\boldsymbol{Z}$, while the existing method [4] solving JE problem for both the image and field map using iterative CG method requires much larger computation time $O(N_1^2 N_2^2)$ per each iteration [21]. The described above HR technique is called the LS Prony method. Other techniques exist to solve the HR problem, such as forward-backward (FB), total LS Prony (TLS), Cadzow denoising, and iterated quadratic maximum likelihood (IQML) methods [19], [20], [22]–[24]. FB method is a variation of LS Prony method, where harmonics are assumed to lie on the unit circle. The rest of the listed methods are HR methods which deal with the noise in the data. Particularly, IQML gives a maximum-likelihood solution to the HR problem and it asymptotically reaches the Cramer-Rao lowest bound on the estimated harmonics as the number of data samples approaches infinity. Its first iteration coincides with the TLS Prony method.

C. Condition on the Field Map Smoothness

In the noiseless case for each fixed n_1 the HR problem (13) solves for each column of $f[n_1, n_2]$ of the image and a corresponding phase sequence

$$\theta_{n_2} = -\angle z_{n_2} = \omega[n_1, n_2]\delta_2 + \frac{2\pi}{N_2}n_2\Delta_2, \quad (19)$$

which we call as the *harmonics*, but the order of θ_{n_2} (and hence, $f[n_1, n_2]$) in general cannot be preserved, since in the HR problem (13) reordering of $\{a_n\}$ and $\{z_n\}$ does not change the data $\{\tau_m\}$. To resolve this ambiguity, we require the sequence $\theta_{n_2} = \omega[n_1, n_2]\delta_2 + \frac{2\pi}{N}n_2\Delta_2$ to be strictly increasing with respect to n_2, *i.e.*

$$\begin{aligned} \omega[n_1, n_2]\delta_2 + \frac{2\pi}{N_2}n_2\Delta_2 &< \omega[n_1, n_2+1]\delta_2 \\ &+ \frac{2\pi}{N_2}(n_2+1)\Delta_2, \end{aligned} \quad (20)$$

which is equivalent to

$$\omega[n_1, n_2] - \omega[n_1, n_2+1] < \frac{2\pi\Delta_2}{N_2\delta_2}, \text{ for all } n_1, n_2. \quad (21)$$

We call this condition the *smoothness* condition, which requires the field map to be sufficiently smooth. Most standard methods of estimating the field map are limited by the overall field map range that they can afford. Instead, here we require a generous smoothness condition (21) on the field map, which in practice is satisfied. For example, given $\delta_2 = 0.5$ ms and 64×64 data samples, the smoothness condition requires $\omega[n_1, n_2] - \omega[n_1, n_2+1] < 393$ rad/s or 62.5 Hz. Thus, in this case our approach only requires the variation in field map of adjacent voxels to be bounded by 62.5 Hz, while the whole variation range of the field map can be as much as 63 times larger.

If the smoothness condition is not satisfied, the HR method will retrieve the harmonics with some local swapping of the order. This will lead mostly to a discontinuity in the recovered image and field map. Since there is not any prior information about the correct order of the harmonics, we check for any

voxel of the recovered image that has discontinuity and we replace its value by an interpolated intensity of the neighbor voxels. This condition rarely happens in the fMRI data that we have collected so far.

Without the field map term, the n_2^{th} harmonic is $2\frac{\pi}{N_2}n_2\Delta_2$. Thus, the smoothness condition is automatically satisfied and plotting all harmonics over n_2 gives a straight line ranging from 0 to 2π. The presence of the field map can be viewed as fluctuations around this straight line. Noise in the field map η_ω can further push some harmonic at position n_2 too close to its neighbor harmonic at $n_2 - 1$ or $n_2 + 1$, which makes the JE problem ill-conditioned or even ill-posed.

When the data $\hat{s}[n_1, m_2]$ are contaminated with noise $\boldsymbol{\eta}$, which is assumed to be additive complex uncorrelated Gaussian noise $\mathcal{N}(\mathbf{0}, \sigma^2\boldsymbol{I})$, then the HR method returns an estimate $\widetilde{\theta}_{n_2}$ of θ_{n_2}. We denote the noisy observations as

$$\boldsymbol{y} = \boldsymbol{s} + \boldsymbol{\eta}, \tag{22}$$

where $\boldsymbol{s}$ is a vector consisting of all signal samples $\hat{s}[n_1, m_2]$, $m_2 = 0, ..., M_2 - 1$. In the case of an unbiased estimator, the harmonic separation $g_{n_2} = \theta_{n_2+1} - \theta_{n_2}$ is the distance $E[\widetilde{\theta}_{n_2+1}] - E[\widetilde{\theta}_{n_2}]$ between the means of two distributions. Thus, assuming uniform distribution in the range $[0; 2\pi]$ for parameters $\widetilde{\theta}_{n_2}$, we can impose the following condition on g_{n_2} so that the two harmonics are resolvable [25]:

$$g_{n_2} \geq \left(\sqrt{CRB_{\theta_{n_2+1}}} + \sqrt{CRB_{\theta_{n_2}}}\right), \tag{23}$$

where $CRB_{\theta_{n_2}}$ is the Cramer-Rao lower bound (CRB) on the variance of the error between estimated $\widehat{\theta}_{n_2}$ and exact parameters θ_{n_2} of the model. This CRB for the HR problem has been studied and derived in the literature (see [26] and other results on CRB in [25], [27]). This condition is just one reasonable necessary condition for g_{n_2}, because if we choose a different resolvability criteria, we will get a different bound on g_{n_2}. Using (19) we get

$$g_{n_2} = \theta_{n_2+1} - \theta_{n_2} = \delta_2(\omega[n_1, n_2 + 1] - \omega[n_1, n_2]) + \frac{2\pi}{N_2}\Delta_2.$$

Substituting this equation into (23) we get the following constraint:

$$\omega[n_1, n_2] - \omega[n_1, n_2+1] \leq \frac{\frac{2\pi\Delta_2}{N_2} - \sqrt{CRB_{\theta_{n_2+1}}} - \sqrt{CRB_{\theta_{n_2}}}}{\delta_2}, \tag{24}$$

which is the smoothness condition in the presence of noise. In [28], a noise fluctuation study on 5 normal subjects was performed to obtain the average value of $SNR(\boldsymbol{y})$ at different spatial resolutions and field strengths. For our case, where the resolution is $3 \times 3 \times 3$ mm^3 and field strength is 3 T, the listed $SNR(\boldsymbol{y})$ was 87.80 or 38.8 dB, where

$$SNR(\boldsymbol{y}) = \frac{||\boldsymbol{s}||_2^2}{||\boldsymbol{s} - \boldsymbol{y}||_2^2} \text{ or } SNR_{dB}(\boldsymbol{y}) = 10\log_{10} SNR(\boldsymbol{y}). \tag{25}$$

At this signal-to-noise ratio and for the same practical values $\delta_2 = 0.5$ ms and 64×64 data samples as we used in the noiseless case, condition (24) requires the lowest allowable value of $\omega[n_1, n_2] - \omega[n_1, n_2 + 1]$ is approximately 60.6 Hz, as shown in Fig. 2. When SNR of $\boldsymbol{y}$ is two times smaller (19 dB), the lowest allowable value of $\omega[n_1, n_2] - \omega[n_1, n_2 + 1]$ decreases to 46.1 Hz. In comparison, the lowest allowable value is 62.5 Hz in the noiseless case. The plots in Fig. 2 were produced from a ground truth image and field map of the subject's brain. We chose a column from a field map low in the brain that ranged from -53.34 Hz to 61.77 Hz, avoiding regions outside the brain.

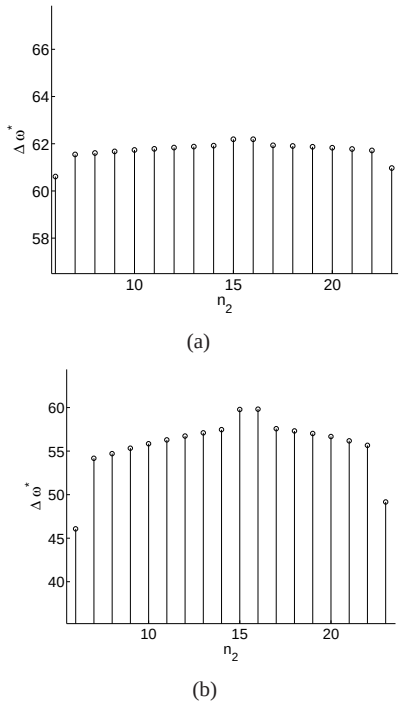

Fig. 2. Upper bound on $\Delta\omega_{n_2}$ in Hz, given $\delta_2 = 0.5$ ms and $N_2 = 64$: (a) SNR of observations $\boldsymbol{y}$ is 38 dB; (b) SNR of observations $\boldsymbol{y}$ is 19 dB. For clarity, only the region of the subject is shown.

D. Proposed Algorithm

Below is the summary of proposed algorithm (see Fig. 3 for illustration):

1) Given acquisition data samples $s[n_1, n_2]$, divide correspondingly by the discrete samples of the function $\Phi_{\mathbf{T}}(\boldsymbol{k})$ and take inverse DFT along m_1 axis or 1D grid if the readout is ramp-sampled. Denote the result by $\hat{s}[n_1, m_2]$.
2) For each fixed value of n_1 solve the 1D HR problem described by (11), (12), and (13) to recover $\omega[\boldsymbol{n}]$, image $\tilde{f}[\boldsymbol{n}]$, and $T_2^*[\boldsymbol{n}]$ map.

IV. METHODS

A. Proposed Acquisition Scheme

As it was mentioned, from (13) it can be seen that $2N$ unknowns from the magnitude and phase of the a_n term, which is the set of all image voxels at a particular column n_1, and $2N$ unknowns from the magnitude and phase of the z_n term, which contain T_2^* and field map values at the n_1^{th} column respectively, lead to the minimum of $2N$ complex data samples τ_m, which are the desired MRI data samples to

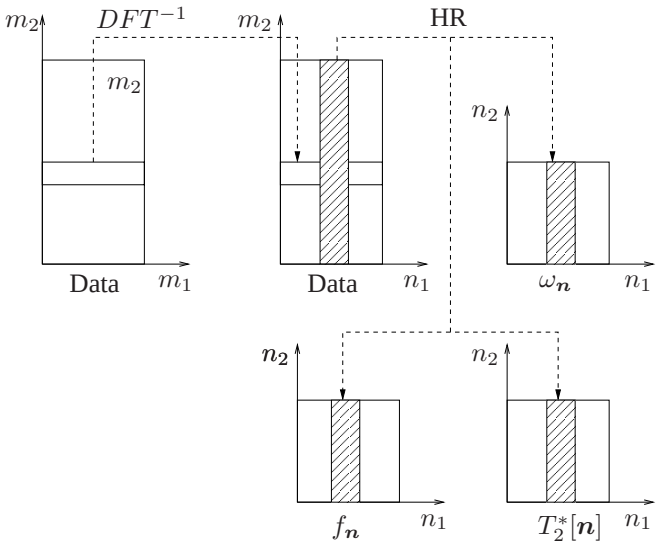

Fig. 3. Illustration of the proposed approach.

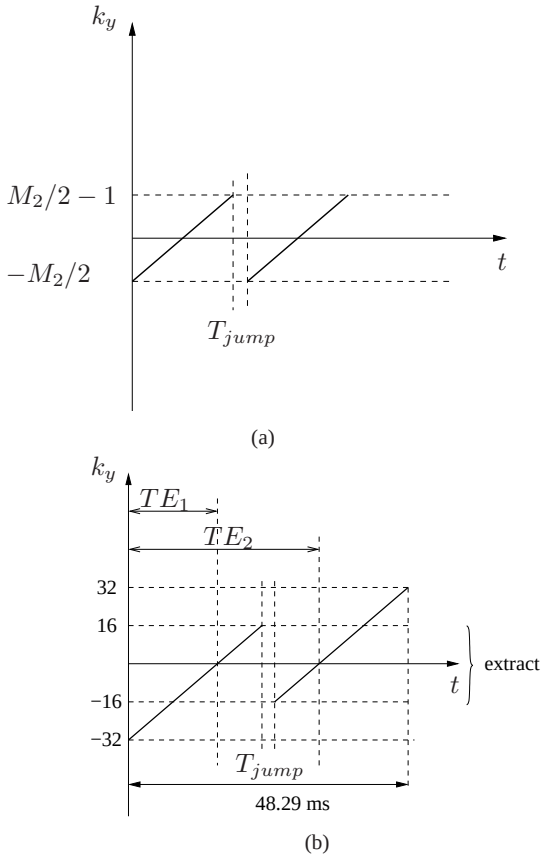

Fig. 4. (a) Proposed k-space trajectory for the HR framework; (b) Proposed interleaved k-space trajectory.

be collected. Hence, HR requires size of the collected data to be larger than the final resolution of the image, field map, and T_2^* map by a factor of 2 along the phase-encoding direction, which motivates for a double-echo acquisition. Standard EPI data is not sufficient for the current HR framework. One way to double the number of k-space lines would be to decrease the spacing Δ_2 in k-space along phase-encoding direction twice, thus getting twice more k-space lines. Although this approach indeed works, it reduces the overall range of ϕ_{n_2} terms from $[0, 2\pi]$ to $[0, \pi]$, which makes the JE problem more ill-conditioned. Instead, consider k-space trajectory shown in Fig. 4(a), where a standard EPI trajectory is centered about the k-space origin and traversed twice. It can be verified that with this trajectory, the equation (6), after making an assumption that $\omega[\boldsymbol{n}]\delta_1 \approx 0$ and $\delta_1/T_2^*[\boldsymbol{n}] \approx 0$ and taking inverse DFT along m_1, becomes

$$\begin{aligned}\hat{s}_1[n_1, m_2] &= \sum_{n_2=0}^{N_2-1} f[n_1, n_2] e^{-m_2\delta_2/T_2^*[n_2]} \\ &\quad \times e^{-i(\omega[\boldsymbol{n}]m_2\delta_2 + \frac{2\pi}{N_2}\Delta_2 n_2 m_2)} \end{aligned} \tag{26}$$

for the first time traversing through the k-space center, i.e. $m_2 = 0, ..., M_2/2 - 1$, and

$$\begin{aligned}\hat{s}_1[n_1, m_2] &= \sum_{n_2=0}^{N_2-1} f[n_1, n_2] e^{-(m_2\delta_2 + T_{jump})/T_2^*[n_2]} \\ &\quad \times e^{-i\left(\omega[\boldsymbol{n}](m_2\delta_2 + T_{jump}) + \frac{2\pi}{N_2}\Delta_2 n_2 (m_2 - \frac{M_2}{2})\right)} \end{aligned} \tag{27}$$

for the second time, where $m_2 = M_2/2, ..., M_2 - 1$ and T_{jump} is the time required to reset the position in k-space between the two passes through the center of k-space. Notice that the desired data by HR, as we discussed, should be

$$\begin{aligned}\hat{s}[n_1, m_2] &= \sum_{n_2=0}^{N_2-1} f[n_1, n_2] e^{-m_2\delta_2/T_2^*[n_2]} \\ &\quad \times e^{-i(\omega[\boldsymbol{n}]m_2\delta_2 + \frac{2\pi}{N_2}\Delta_2 n_2 m_2)} \end{aligned} \tag{28}$$

for both the first and second halves of the data, i.e. $m_2 = 0, ..., M_2 - 1$. Hence, the first half of the data produced with the considered k-space trajectory is the same as the first half of the data that the HR framework needs. We further notice that the term $\frac{2\pi}{N_2}\Delta_2 n_2 (m_2 - \frac{M_2}{2})$ in (27) can be simplified to $\frac{2\pi}{N_2}\Delta_2 n_2 m_2$ when M_2 is a multiple of $2N_2$. In this case, comparing (26) and (27) with (28), the considered trajectory satisfies the HR framework when $T_{jump} = 0$. We keep T_{jump} short to try to minimize its effect on the estimation scheme. In our sequence T_{jump} is 420 μs, which is small on the order of one δ_2.

We can further extend our proposed k-space trajectory as shown in Fig. 4(b), so that we could also obtain a higher resolution standard EPI data and then use them together with the obtained from HR image and field map of a lower resolution to fit the iterative CG reconstruction proposed in [4]. Note that the magnitude MR image, field map, and T_2^* map can all be calculated from the sequence illustrated in Fig. 4(b) using conventional post-processing methods.

The sequence parameters are the following: dwell time $\delta_1 = 3.4$ μs, echo spacing $\delta_2 = 0.5$ ms, echo times $TE_1 = 25$ ms and $TE_2 = 41$ ms, $T_{jump} = 420$ μs, $TR = 2$ s, and a stack of 20 2D slices is acquired every TR. Specifically, to acquire 64×64 MRI data, we consider k-space window (k-space is normalized by $\frac{1}{FOV}$) $-32 \leq k_x \leq 32$ and $-32 \leq k_y \leq 32$. In that k-space region we cover the first subregion $-32 \leq k_y \leq 16$ along a standard EPI trajectory (by

alternating the polarity of the readout gradient and applying the phase-encoding gradient blips) and then the second subregion $-16 \leq k_y \leq 32$ also along the same trajectory. Then, the data from both the first and the second subregions that fall within the range $-16 \leq k_y \leq 16$ are extracted and stacked. By doing this we get the two k-space subregions interleaved and the extracted 64×64 data represents the oversampling of k-space center. We should also point out that in practice we use ramp-sampling in the k_x direction along with oversampling, providing a more time efficient EPI readout. So instead of getting 64 sampled along k_x direction, we get 128 samples within the range $-32 \leq k_x \leq 32$. Then, we use the gridding procedure [29] to generate 64 uniformly spaced image locations across the field of view in the x-direction. At the end of the acquisition window we apply the spoiler to spoil residual magnetization to prepare for the excitation of the next slice.

At the beginning of the EPI readout, we collect 3 lines (2 forward and 1 backward) at $k_y = 0$ for correcting ghosting artifact, which is caused mainly by eddy currents. Eddy currents cause odd and even echo lines to have an alternating shift in the k-space along the frequency encoding direction, which in turn leads to the phase ramps in the image domain, visualized as a ghost effect. Acquiring reference lines with no phase encoding helps to estimate and remove this effect. We used the standard single pair, 3 reference line method to correct for Nyquist ghost, where the first and third lines were averaged together to obtain an average forward line with the same echo time as the single backward line (refer to [30]).

Along with the mentioned advantages of the proposed acquisition scheme, there are trade-offs. One obvious disadvantage is the reduction of the number of slices that could fit within a TR time interval, since the acquisition time per each slice increases compared with the conventional gradient-echo EPI sequence. For a conventional EPI sequence, the echo time is 25 ms and there is a half of k-space left to acquire after the echo, i.e. 16 ms. Given a 2 ms RF pulse (of which half counts towards TE), the total time for a single slice would be $(1+25+16) = 42$ ms. For our proposed acquisition, recall that the first echo time is 25 ms and the second is 41 ms. With 16 ms of additional data acquisition after the last echo, the total scan time per slice now is $(1 + 41 + 16) = 58$ ms, which is an increase of 16 ms compared to the normal EPI acquisition. Thus, the number of slices that could be scanned will decrease. Second trade-off is that the acquisition will experience a more significant T_2^* decay, especially the second half of the data. This is a main reason for the signal loss in the acquisition. Note that we are modeling voxels as having constant field map, so any gradients would result in a decrease in T_2^* value for that voxel. We may not be able to estimate the signal from the regions of a severe signal decay, which is faster than the echo time of our sequence.

B. Regularization

Recall equation (12), from which we see that the T_2^* map can be estimated as the following:

$$T_2^*[\boldsymbol{n}] = -\delta_2 / \ln |z_{\boldsymbol{n}}|. \tag{29}$$

Due to the characteristics of the logarithmic function in the region when $|z_{\boldsymbol{n}}| \leq 1$, small perturbations in $|z_{\boldsymbol{n}}|$ lead to large perturbations in the $T_2^*[\boldsymbol{n}]$ value, which implies the need of the regularization in the case of high noise level in the data. In practice the $T_2^*[\boldsymbol{n}]$ map has values ranging in the order of 10 ms to 100 ms, which means that in the case $\delta_2 = 0.5$ ms, the magnitude of $z_{\boldsymbol{n}}$ is $e^{-\delta_2/T_2^*[\boldsymbol{n}]} = 0.95$ and 0.995, respectively. This fact is taken as a prior knowledge about $|z_n|$ and incorporated into the JE model.

Suppose that $|z_n| = \alpha$. Using similar arguments as in the Forward-Backward algorithm [19] we can show that in addition to the matrix equation (17) we have the following equation:

$$\underbrace{\begin{bmatrix} \tau_N^* c_N^*(\boldsymbol{\alpha}) & \tau_{N-1}^* c_{N-1}^*(\boldsymbol{\alpha}) & \dots & \tau_1^* c_1^*(\boldsymbol{\alpha}) \\ \tau_{N+1}^* c_N^*(\boldsymbol{\alpha}) & \tau_N^* c_{N-1}^*(\boldsymbol{\alpha}) & \dots & \tau_2^* c_1^*(\boldsymbol{\alpha}) \\ & \dots & & \\ \tau_{M-2}^* c_N^*(\boldsymbol{\alpha}) & \tau_{M-3}^* c_{N-1}^*(\boldsymbol{\alpha}) & \dots & \tau_{M-N-1}^* c_1^*(\boldsymbol{\alpha}) \end{bmatrix}}_{\boldsymbol{A_\alpha}} \times \underbrace{\begin{bmatrix} p_0 \\ p_1 \\ \dots \\ p_{N-1} \end{bmatrix}}_{\boldsymbol{p}} = -\underbrace{\begin{bmatrix} \tau_0^* c_0^*(\boldsymbol{\alpha}) \\ \tau_1^* c_0^*(\boldsymbol{\alpha}) \\ \dots \\ \tau_{M-N-2}^* c_0^*(\boldsymbol{\alpha}) \end{bmatrix}}_{\boldsymbol{b_\alpha}}, \tag{30}$$

where

$$\boldsymbol{c}(\boldsymbol{\alpha}) = \begin{bmatrix} (\alpha^N)^*/\alpha^0 & (\alpha^{N-1})^*/\alpha^1 & \dots & (\alpha^0)^*/\alpha^N \end{bmatrix}^T. \tag{31}$$

A least squares solution for (17) and (30) can be formulated as the solution to the optimization problem

$$\min_{\boldsymbol{p}} \left\{ ||\boldsymbol{A}\boldsymbol{p} - \boldsymbol{b}||^2 + \lambda^2 ||\boldsymbol{A}_{\boldsymbol{\alpha}}\boldsymbol{p} - \boldsymbol{b}_{\boldsymbol{\alpha}}||^2 \right\}, \tag{32}$$

where parameter λ determines the significance of the constraint $|z_n| = \alpha$; the larger λ, the more significant the constraint is. When $\lambda = 0$, we return to the general joint estimation problem without any constraint. Notice that for a special case when $\alpha = 1$, which means that all $\{z_n\}$ lie on the unit circle, and $\lambda = 1$, the matrix equation (30) becomes the same as in the Forward-Backward method. The solution to (32) is obtained by solving the least-squares solution of the following matrix equation for the coefficients $\{p_i\}$:

$$\begin{bmatrix} \boldsymbol{A} \\ \lambda \boldsymbol{A}_{\boldsymbol{\alpha}} \end{bmatrix} \boldsymbol{p} = \begin{bmatrix} \boldsymbol{b} \\ \lambda \boldsymbol{b}_{\boldsymbol{\alpha}} \end{bmatrix}. \tag{33}$$

Having the coefficients $\{p_i\}$, the desired regularized $\{z_n\}$ can be found as the roots of the characteristic polynomial (16).

V. EXPERIMENTAL RESULTS

A. Simulated Data

To quantify performance of the proposed approach we simulate data with realistic field maps. In these experiments, a real MRI image and field map were acquired in accordance with the Institutional Review Board (IRB) of the University of

Illinois at Urbana-Champaign. The ground truth field map was obtained by a non-fMRI, multi-echo GRE (not EPI) acquisition with $TR = 400$ ms, flip angle of $45°$, echo times 10 ms and 12.46 ms. The acquisition gives the correct field map, although it takes about 2 mins to acquire. In addition, the resulting image from this acquisition does not have the same contrast as the functional image and does not contain function information.

The MRI data is simulated according to the model described in (10) and (14) with the following parameters: $\Delta_1 = \Delta_2 = 1$, $\delta_1 = 5$ μs, $\delta_2 = 400$ μs and the T_2^* map is also synthesized. We are interested in the SNR of the reconstructed image with and without compensating for the field map and the SNR of the field map recovered from conventional field map estimation and our joint estimation. The conventional field map estimation that we compare our method to is based on reconstructing the individual images from the oversampled central k-space lines and dividing their phase difference by the difference in echo times, which was 16 ms in this case.

In the first experiment, the input image to the algorithm is an axial slice of the brain and the corresponding field map shows a significant off-resonance due to field inhomogeneity in the region of the frontal lobe, as shown in Fig. 5(a),(f). The field map varies from -10.34 Hz until 40.44 Hz. In this experiment the T_2^* map was modeled as ovals (see Fig. 5(i)). The T_2^* value for the gray and white matters was taken to be 80 ms (the region outside the two ovals) and 50 ms (the region inside the two ovals) respectively, according to [31].

The results, given in Fig. 5, show that our approach recovers the original image and field map better (SNR = 61.02 dB for the image and SNR = 31.35 dB for the field map) compared to the case where field map is not considered (SNR = 20.48 dB for the image). Note that for an appropriate SNR comparison with the HR image reconstruction, the DFT recovered image does not include T_2^* decay. The total acquisition time along the phase-encoding direction is $N_2 \times \delta_2 = 64 \times 0.5$ ms= 32 ms, which leads to the bandwidth per pixel $BWPP_{pe} = 31.3$ Hz along the phase-encoding direction. Since the field map is moderate and has a maximum value of 40.44 Hz, we expect there is about 1 to 2 off-pixel shifts, which is not noticeable from the image in Fig. 5(c). The distortion along the frequency encoding direction is negligible because δ_1 is very small. For a clear visualization, Fig. 5(d) shows the difference between the HR recovered and original images and Fig. 5(e) shows the difference between the DFT reconstructed image and the original image. Conventional field map estimate results from the distorted image, so its contour is also slightly distorted as can be seen from Fig. 5(h). In addition, the regions of white and grey matter in the T_2^* map recovered by HR, shown in Fig. 5(j), resemble those regions in the ground truth T_2^* map with SNR=20.93 dB.

In the second simulation experiment, shown in Fig. 6, the phantom is filled with two horizontal plastic structures inside and the ground truth field map is more severe. This field map has a maximum absolute value of 71 Hz, which causes a geometric distortion in the region of field inhomogeneity to a reconstructed image without taking into account the field map. The T_2^* ground truth was simulated to be a 10 ms constant map. For this particular experiment, the field map and the T_2^* decay are more severe than in the first case. We apply the proposed in the section IV-B regularization approach with the regularization parameters $\alpha = e^{-\delta_2/10\text{ms}} = 0.95$ and $\lambda = 1$. The results are shown in Fig. 6. While the recovered from HR magnituge image resembles the original image perfectly with SNR=40.85 dB (Fig. 6(b)), the DFT reconstruction is visually worse and has SNR=15.89 dB. As we can see from Fig. 6(c), compared to the original image, the two stripes in the DFT reconstructed image are skewed off by some small angle towards the top of the image with the maximum extend in the right area where the ground truth field map is most significant. The maximum distortion in the phase encode direction should be approximately 3 pixels (90 Hz/$BWPP_{pe}$), which is approximately what we observe. To visualize this skewing clearer, Fig. 6(d) shows the difference between the original image and the DFT reconstructed image. Note that for a fair comparison with the HR reconstruction, the DFT reconstructed image does not have a T_2^* weighting included, similar to the first simulation. The field map recovered from our approach has SNR = 24.53 dB and its original shape and all details are more preserved than a conventional field map estimate, which has a slightly distorted shape and the stripes slightly shifted from their original positions. In addition, our approach retrieves a T_2^* map that is very close to the 10 ms constant ground truth, as shown in Fig. 6(h). We further gradually scaled the ground truth T_2^* maps in both experiments shown in Fig. 5 and Fig. 6 and found that the T_2^* value below 1 ms gives a very severe signal loss to the MRI data, especially to the second half of the data, leading to an impossible retrieval of the desired image, field map, and T_2^* map.

B. Real Data

Results of our technique applied on two real subjects together with the DFT reconstructed image and field map, obtained by applying the conventional field map estimate approach that has been described in Simulated data section, are displayed in Fig. 7 and Fig. 8. For each experiment 20 axial slices 3 mm thick at 25 time points with a TR of 2 s were acquired using the proposed acquisition scheme. Severeness of field inhomogeneity increases when we go from slice 20 (superior) to slice 1 (inferior). The T_1-weighted reference image and ground truth field map were acquired with the non-fMRI GRE acquisition described in the section V-A ($TE = 10$ ms, 12.46 ms) that is not significantly geometrically distorted by the field inhomogeneity. Acquisition time for this static field map was approximately 2 min. Notice that although the T_1-weighted reference image is insensitive to magnetic field inhomogeneity, it is also insensitive to functional changes leading to a different contrast in the image. Thus, we use the reference image only as a ground truth for the overall geometric shape of the object.

As the second simulation study suggests, for the real data case with some the noise level, the problem becomes badly ill-conditioned and thus we need to apply regularization in order to solve for the reasonable image, field map, and T_2^* map. Before applying the regularization approach proposed

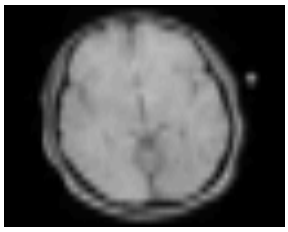

(a) Original 64×64 image.

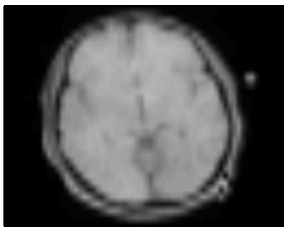

(b) HR recovered image, SNR = 61.02 dB.

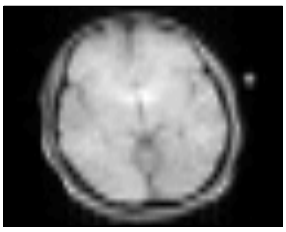

(c) DFT recovered image without T_2^* decay, SNR=20.48 dB.

(d) Error of HR reconstruction: 5(a)-5(b).

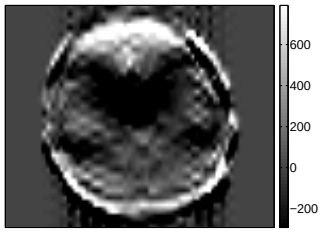

(e) Error of DFT reconstruction: 5(a)-5(c).

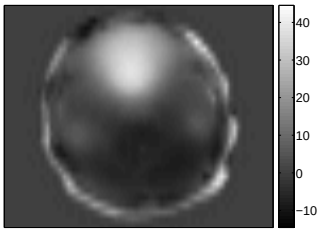

(f) Original field map.

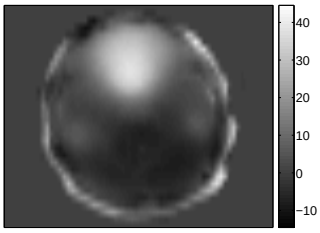

(g) HR recovered field map, SNR = 31.35 dB.

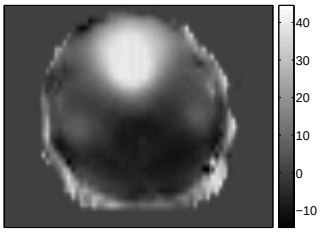

(h) Conventional field map estimation.

(i) Synthesized T_2^* map in seconds.

(j) HR recovered T_2^* map in seconds, SNR=20.93 dB.

Fig. 5. Simulation 1: reconstructions. All scales of field maps are in Hz.

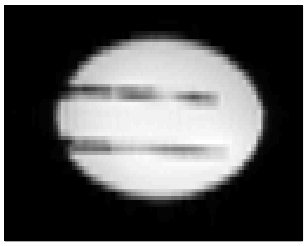

(a) Original 64×64 image.

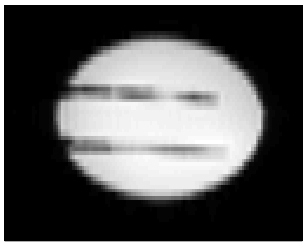

(b) HR recovered image, SNR = 40.85 dB.

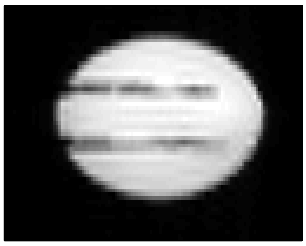

(c) DFT recovered image without T_2^* decay, SNR=15.89 dB.

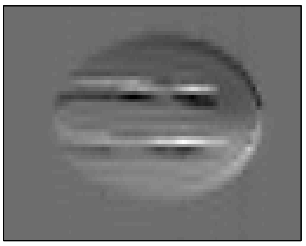

(d) 6(a)-6(c).

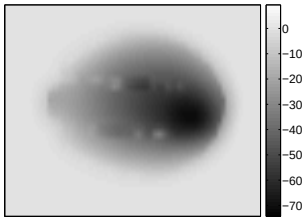

(e) Original field map.

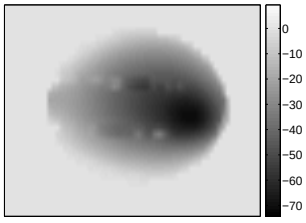

(f) HR recovered field map, SNR = 24.53 dB.

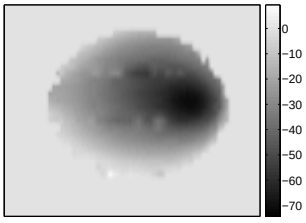

(g) DFT recovered field map.

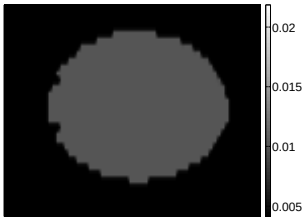

(h) HR recovered T_2^* map in seconds.

Fig. 6. Simulation 2. All scales of field maps are in Hz.

in the section IV-B, we need to decide which value of the regularization parameters α and λ, introduced in (32), to take. As already discussed, parameter λ is used to enforce the level of significance of the constraint $|z_n| = \alpha$, while parameter α plays a crucial role on the reconstruction. In fact, the acquired MRI data contain a rough idea about the value of α. The data acquired from the proposed gradient-echo sequence always have two data peaks, which we denote as S_1 and S_2, each

corresponding to the time when the echo appears. Since the amplitude of a gradient echo carries a mean T_2^*-weighting, we fit an exponential through the signal intensities of these two data peaks. Thus, the mean T_2^* value can be estimated as

$$\widetilde{T}_2^* = \frac{TE_1 - TE_2}{\ln(S_2/S_1)} \tag{34}$$

and based on (15) we choose α to be $e^{-\delta_2/\widetilde{T}_2^*[\boldsymbol{n}]}$. However, note that this is only a rough, poor estimate of α. After the HR reconstruction, it is possible to detect the HR failures from the information about $|z_{n_2}|$ for each fixed n_1. Specifically, if the recovered $|z_{n_2}|$ values are out of the possible physical range, i.e. $|z_{n_2}| > 1$ (outside of unit circle) or $|z_{n_2}| < \epsilon$, where ϵ is the threshold dictated by the smallest possible T_2^* value, taken from the prior information about the T_2^* range, then at the corresponding recovered HR image pixels we will see the dark or white gaps, respectively. We correct these pixels by setting the value of $|z_{n_2}|$ to either 1 or ϵ, which automatically corrects for the T_2^* map. If this still gives an obvious failure in the reconstructed image, we interpolate the nearest neighbor pixels of the image at that location.

Figure 7 shows the reconstructions of a lower slice covering the medial temporal lobe, where field inhomogeneity begins to have a dramatic effect on the usual DFT image reconstruction (field map varies from -73.63 Hz to 35.21 Hz in this slice). As discussed, at those locations that the HR approach fails to recover $|z_n|$ in the reasonable range, we threshold the wrongly recovered $|z_n|$ and apply the interpolationg on the neigbor image pixels. Shown in Fig. 7(a) is the DFT image reconstruction, while Fig. 7(b) shows the HR image reconstruction when the regularization parameter α is set to 0.99 and $\lambda = 1.7$, which gives a good image reconstruction with a trade-off on the field map and T_2^* reconstructions. In the middle region of the brain where there is a signal void, indicated by an arrow, the proposed approach succeedes to fill in the image. Fig. 7(d) shows the corresponding T_2^* map reconstruction. The reconstructed T_2^* map is smooth and varies in the range from 20 ms to 50 ms, with the most common values of 46 ± 3 ms. Figs. 7(e),(f) show a conventionally estimated field map and a HR recovered field map, both beging not phase unwrapped except for a very obvious 2π wraps, where we use the available information from the neigbor, not-phase wrapped, field map columns to compensate for the wraps. Phase unwrapping for the HR field map reconstruction remains to be the future work and is out of scope of this paper.

Similar to the first experiment, reconstructions from the second real experiment are shown in Fig. 8. Arrows in Fig. 8(a) indicate those regions of the brain that are corrected using the HR approach with the regularization parameter α and λ being equal to 0.985 and 1, respectively. Recall again from our discussion that in the proposed approach, the term $|z_{n_2}|$ carries a significant amount of information, since it helps to identify those image and T_2^* voxels at which HR fails. This enables a post-processing step to correct for these failures. Recovered by the HR, the T_2^* map, shown in Fig. 8(d), has the maximum value of 50 ms, with the most common value range from 28 ms to 34 ms approximately, which is fairly relevant to the estimated value of 33 ms found by fitting an exponential. In the region of the severe signal decay the recovered T_2^* value drops to 2 ms. This results in recovery of signal in the region corresponding to the low T_2^* area, as seen from the reconstructed HR image. Figs. 8(e),(f) show the unwrapped field maps, reconstructed from the conventional and HR approaches.

Dynamic imaging study was performed on the same two subjects to assess the stability of the proposed approach. To show the image intensity fluctuations over all voxels, we take the time series of reconstructions, demean whole data with respect to time, and then for each voxel we calculate the normalized root mean squared error (NRMSE) around the corresponding mean to obtain the NRMSE map which quantifies the signal fluctuations over time. Larger fluctuations of the reconstructed signals over time result in a higher NRMSE. Figs. 9(a),(b) show the NRMSE maps for the HR and DFT reconstructed images for the first real data experiment. These two maps indicate that both DFT and HR approaches have small signal fluctuations over the time, fairly comparable to each other. The bright spots in Fig. 9(a) show the locations at which the ill-conditioning of the HR method is more significant than at the other locations. For the second subject, as can be seen from Figs. 10(a),(b), variations in the HR signal are larger and in this case DFT stability outperforms the HR stability. The T_2^* NRMSE maps for the two subjects are shown in Fig. 9(c) and Fig. 10(c), respectively. These plots suggest that the T_2^* map reconstruction is fairly stable over time and is more stable than the HR image reconstruction. This can be explained from the fact that the T_2^* map relates directly to the recovered from HR $|z_n|$ according to (29), while the magnitude image is found from $|z_n|$ by inverting Vandermond matrix, which causes the ill-conditioning in the image reconstruction. It is worth pointing out that the HR method is non-iterative: it does not use any information about previous time points nor does it smooth temporally. Overall, the pixel-wise signal fluctuations were not in a large scale, although a further improvements on the stability of the HR method should be investigated.

VI. CONCLUSION

In this work, we propose a new, non-iterative method for joint estimation (JE) and correction of susceptibility artifacts problem in the case of EPI functional MRI. We present a method that can dynamically estimate the undistorted field map, magnitude image, and T_2^* map simultaneously from the acquired multi-echo EPI data, non-iteratively. The advantages of this approach are: (i) much lower complexity compared with a recent method [4] which views the JE problem as a nonlinear least-squares optimization problem; (ii) this approach does not require a prior knowledge of the field map.

We convert the JE problem to the harmonic retrieval (HR) problem by making a practical approximation that helps to transform the nonlinear 2D JE problem to a set of 1D linear problems. To make a bridge between the JE and HR problems, we need a generous condition, which we call the smoothness condition, on the smoothness voxel-to-voxel along vertical

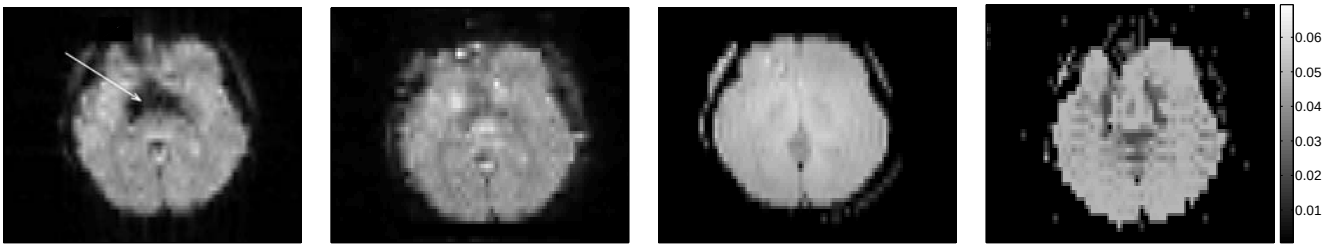

(a) DFT reconstructed image. (b) HR reconstructed image. (c) Reference image. (d) HR reconstructed T_2^* map (in sec).

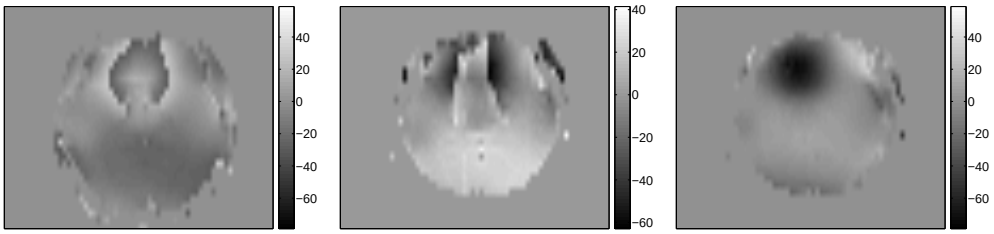

(e) Conventional field map estimate (unwrapped). (f) HR reconstructed field map (unwrapped). (g) Ground truth field map.

Fig. 7. Experimental results with the first subject. HR magnitude image, field map, and T_2^* reconstructions are obtained with the regularization parameters $\alpha = 0.99$ and $\lambda = 1.7$. All scales of field maps are in Hz.

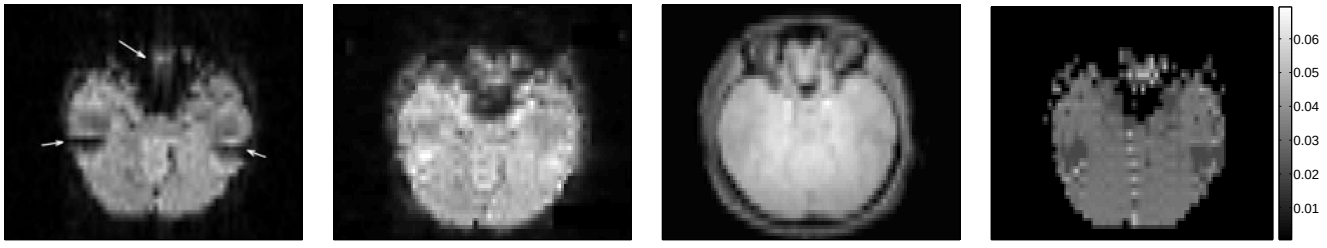

(a) DFT reconstructed image. (b) HR reconstructed image. (c) Reference image. (d) HR reconstructed T_2^* map in sec.

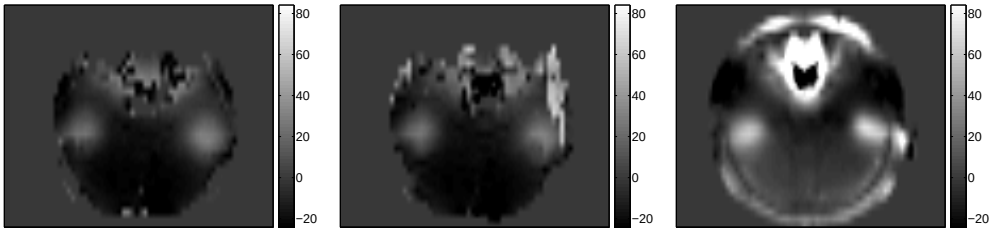

(e) Conventional field map estimate (unwrapped). (f) HR reconstructed field map (unwrapped). (g) Ground truth field map.

Fig. 8. Experimental results with the second subject. HR magnitude image, field map, and T_2^* reconstructions are obtained with the regularization parameters $\alpha = 0.985$ and $\lambda = 1$. All scales of field maps are in Hz.

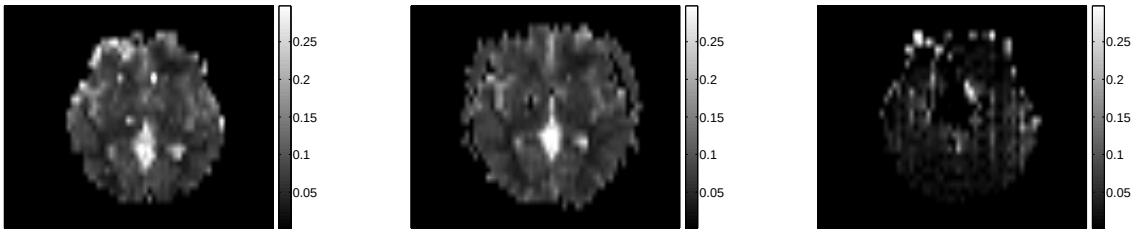

(a) (b) (c)

Fig. 9. Dynamic imaging study with the first subject: normalized root mean squared error (NRMSE) map for (a) HR image reconstruction; (b) DFT image reconstruction; (c) HR T_2^* map reconstruction.

direction of the original field map. In the rare case when the smoothness condition does not hold, we can still reconstruct

(a) (b) (c)

Fig. 10. Dynamic imaging study with the second subject: normalized root mean squared error (NRMSE) map for (a) HR image reconstruction; (b) DFT image reconstruction; (c) HR T_2^* map reconstruction.

all details and shape of the image, but with slight voxel shifts caused by incorrect order of harmonics. A further postprocessing to detect and shift back the voxels can be applied. We analyze the noise effect on the performance of the method and derive a bound on the resolution of the image and size of the field map given a fixed noise level in the case of unbiased estimator. In real practice when the problem becomes ill-conditioned, we propose a specific regularization approach on the apriori known possible range of the T_2^* map. Experimental results on the real data show that the reconstructed from HR image has much reduced signal loss artifact in those regions of the brain that correspond to the low T_2^* area and high field inhomogeneity, as the DFT reconstructed image. A validation of whether and how the proposed regularization affects time-domain signal behavior and BOLD detectability is needed to be performed.

REFERENCES

[1] Z.-P. Liang and P. C. Lauterbur, *Principles of Magnetic Resonance Imaging: A Signal Processing Perspective*, 1st ed. New York: IEEE Press, 2000.

[2] H. Chang and J. M. Fitzpatrick, "A technique for accurate magnetic resonance imaging in the presence of field inhomogeneties," *IEEE Trans. Med. Imaging*, vol. 11, pp. 319–329, Sep. 1992.

[3] T. K. Truong, B. D. Clymer, D. W. Chakeres, and P. Shmalbrock, "Three-dimensional numerical simulations of susceptibility-induced magnetic field inhomogeneities in the human head," *Magn. Res. Imaging*, vol. 20, pp. 759–770, 2002.

[4] B. P. Sutton, D. C. Noll, and J. A. Fessler, "Dynamic field map estimation using a spiral-in/spiral-out acquisition," *Magn. Reson. Med.*, vol. 51, pp. 1194–1204, 2004.

[5] V. Roopchansingh, R. W. Cox, A. Jesmanowics, B. D. Ward, and J. S. Hyde, "Single-shot magnetic field mapping embedded in echo-planar time-course imaging," *Magn. Reson. Med.*, vol. 50, pp. 839–843, 2003.

[6] K. Nayak and D. G. Nishimura, "Automatic field map generation and off-resonance correction for projection reconstruction imaging," *Magn. Reson. Med.*, vol. 43, pp. 151–154, 2000.

[7] E. Schneider and G. Glover, "Rapid in vivo proton shimming," *Magn. Reson. Med.*, vol. 18, pp. 335–347, 1991.

[8] D. C. Noll, G. H. Meyer, J. M. Pauly, D. G. Nishimura, and A. Macovski, "A homogeneity correction method for magnetic resonance imaging with time-varying gradients." *IEEE Trans. Med. Imaging*, vol. 10, pp. 629–637, Dec 1991.

[9] P. Jezzard and R. S. Balaban, "Correction for geometric distortion in echo planar images from B_0 field variations," *Magn. Reson. Med.*, vol. 33, pp. 65–73, 1995.

[10] Y. M. Kadah and X. Hu, "Simulated phase evolution rewinding (SPHERE): a technique for reducing B_0 inhomogeneity effects in MR images," *Magn. Reson. Med.*, vol. 38, pp. 615–627, 1997.

[11] H. Schomberg, "Off-resonance correction of MR images," *IEEE Trans. Med. Imaging*, vol. 18, pp. 481–495, June 1991.

[12] L. C. Man, J. M. Pauly, and A. Macovski, "Multifrequency interpolation for fast off-resonance correction," *Magn. Reson. Med.*, vol. 37, pp. 785–792, 1997.

[13] T. B. Harshbarger and T. Twieg, "Iterative reconstruction of single-shot spiral MRI with off resonance." *IEEE Trans. Med. Imaging*, vol. 18, pp. 196–205, Mar 1999.

[14] B. P. Sutton and J. A. Fessler, "Fast, iterative, field-corrected image reconstruction for MRI." *IEEE Trans. Med. Imaging*, vol. 22, pp. 178–188, Feb 2003.

[15] J. M. S. Hutchinson, R. J. Sutherland, and J. R. Mallard, "NMR imaging: Image recovery under magnetic field with large non-uniformities," *J. Phys., E: Sci. Instrum.*, vol. 11, pp. 217–222, Mar. 1978.

[16] P. S. Morgan, R. Q. Bowtell, D. J. O. McIntyre, and B. S. Worthington, "Correction of spatial distortion in EPI due to inhomogeneous static magnetic fields using the reversed gradient method," *J. Magn. Res. Imaging*, vol. 19, pp. 499–507, 2004.

[17] D. B. Twieg, "Parsing local signal evolution directly from a single-shot MRI signal: a new approach for fMRI," *Magn. Reson. Med.*, vol. 50, pp. 1043–1052, 2003.

[18] H. M. Nguyen, R. Morrison, B. Sutton, and M. N. Do, "Joint estimation in MRI using harmonic retrieval methods," in *IEEE International Symposium on Biomedical Imaging*, 2006, p. 53.

[19] M. Elad, P. Milanfar, and G. H. Golub, "Shape from moments - an estimation theory perspective," *IEEE Trans. Sig. Process.*, vol. 52, pp. 1814–1829, July 2004.

[20] F. B. Hilderbrand, *Introduction to Numerical Analysis*, 2nd ed. New York: Dover, 1974.

[21] D. P. Bertsekas, *Nonlinear Programming*, 2nd ed. Athena Scientific, 1999.

[22] Y. Bresler and A. Macovski, "Exact maximum likelihood parameter estimation of superimposed exponential signals in noise," *IEEE Trans. Acoust. Speech Sig. Process.*, vol. 34, pp. 1081–1089, 1986.

[23] I. Maravic and M. Vetterli, "Sampling and reconstruction of signals with finite rate of innovation in the presence of noise," *IEEE Trans. Sig. Process.*, vol. 53, pp. 2788–2805, Aug. 2005.

[24] J. A. Cadzow, "Signal enhancement - a composite property mapping algorithm," *IEEE Trans. Acoust. Speech Sig. Process.*, vol. 36, pp. 49–62, Jan 1988.

[25] S. F. Yau and Y. Bresler, "Worst case Cramer-Rao bounds for parametric estimation of superimposed signals with applications," *IEEE Trans. Sig. Process.*, vol. 40, pp. 2973–2986, Dec. 1992.

[26] P. Stoica and A. Nehorai, "MUSIC, maximum likelihood, and Cramer-Rao bound," *IEEE Trans. Acoust. Speech Sig. Process.*, vol. 37, pp. 720–741, May 1989.

[27] J. C. Ye, Y. Bresler, and P. Moulin, "Cramer-Rao bounds for parametric shape estimation in inverse problems," *IEEE Trans. Image Process.*, vol. 12, pp. 71–84, Jan. 2003.

[28] C. Triantafyllou, R. D. Hoge, G. Krueger, C. J. Wiggins, A. Potthast, G. C. Wiggins, and L. L. Wald, "Comparison of physiological noise at 1.5T, 3T and 7T and optimization of fMRI acquisition parameters," *NeuroImage*, vol. 26, pp. 243–250, 2005.

[29] J. I. Jackson, C. H. Meyer, D. G. Nishimura, and A. Macovski, "Selection of a convolution function for Fourier inversion using gridding," *IEEE Trans. Med. Imaging*, vol. 10, pp. 473–478, Sep. 1991.

[30] P. Jezzard and S. Clare, "Sources of distortion in functional MRI data," *Human Brain Mapping*, vol. 8, pp. 80–85, Sep 1999.

[31] G. J. Stanisz, "T_1, T_2 relaxation and magnetization transfer in tissue at 3T," *Magn. Reson. Med.*, vol. 54, pp. 507–512, 2005.